Dynamic molecular switches with hysteretic negative differential conductance emulating synaptic behaviour

Yulong Wang [1,9], Qian Zhang[1,8,9], Hippolyte P. A. G. Astier[1,9], Cameron Nickle[2,9], Saurabh Soni [3], Fuad A. Alami [3], Alessandro Borrini [3], Ziyu Zhang[1], Christian Honnigfort[4,5], Björn Braunschweig[4,5], Andrea Leoncini[1], Dong-Cheng Qi [6], Yingmei Han[1], Enrique del Barco [2] ✉, Damien Thompson [7] ✉ & Christian A. Nijhuis [1,3] ✉

To realize molecular-scale electrical operations beyond the von Neumann bottleneck, new types of multifunctional switches are needed that mimic self-learning or neuromorphic computing by dynamically toggling between multiple operations that depend on their past. Here, we report a molecule that switches from high to low conductance states with massive negative memristive behaviour that depends on the drive speed and number of past switching events, with all the measurements fully modelled using atomistic and analytical models. This dynamic molecular switch emulates synaptic behavior and Pavlovian learning, all within a 2.4-nm-thick layer that is three orders of magnitude thinner than a neuronal synapse. The dynamic molecular switch provides all the fundamental logic gates necessary for deep learning because of its time-domain and voltage-dependent plasticity. The synapse-mimicking multifunctional dynamic molecular switch represents an adaptable molecular-scale hardware operable in solid-state devices, and opens a pathway to simplify dynamic complex electrical operations encoded within a single ultracompact component.

Inspired by the energy efficiency of brains and the ever-increasing demand for miniaturized electronics, there is a drive to develop devices that mimic the dynamic character of neurons and synapses to create trainable, adaptive computing networks or new hardware for deep learning for various applications, which include pattern recognition, classification or to realize non-von Neumann neuromorphic computation[1–5]. Neuromorphic computing revolves around emulating synaptic plasticity in electronic systems. Such operations are currently performed using complex, energy-inefficient silicon-based circuits with large footprints, or mesoscale memristive systems based on ferroelectric[6] or phase-change materials[7], filaments or the migration of dopants[1,3,8,9]. In this context, molecular switches are appealing because

[1]Department of Chemistry, National University of Singapore, Singapore, Singapore. [2]Department of Physics, University of Central Florida, Orlando, FL, USA. [3]Hybrid Materials for Opto-Electronics Group, Department of Molecules and Materials, MESA+Institute for Nanotechnology, Molecules Center and Center for Brain-Inspired Nano Systems, Faculty of Science and Technology, University of Twente, Enschede, the Netherlands. [4]Institute of Physical Chemistry, Westfälische Wilhelms-Universität Münster, Münster, Germany. [5]Center of Soft Nanoscience, Westfälische Wilhelms-Universität Münster, Münster, Germany. [6]School of Chemistry and Physics, Queensland University of Technology, Brisbane, Queensland, Australia. [7]Department of Physics, Bernal Institute, University of Limerick, Limerick, Ireland. [8]Present address: School of Chemistry and Chemical Engineering, Chongqing University, Chongqing, China. [9]These authors contributed equally: Yulong Wang, Qian Zhang, Hippolyte P. A. G. Astier, Cameron Nickle. ✉e-mail: delbarco@ucf.edu; damien.thompson@ul.ie; c.a.nijhuis@utwente.nl

of their inherently small size, but molecular switches so far are static, which means they switch between fixed on and off states (such as magnetic, redox or conformational states)[10–12]. Here we report a dynamic molecular switch (DMS) in a tunnel junction that remembers its history, whereby the switching probability and the values of the on and off states continually change. This dynamic switch successfully emulates synaptic behaviour, Pavlovian learning and, by exploiting the time-domain plasticity of the junctions, mimics all the two-terminal logic gates necessary for deep learning. These functionalities are provided within a single molecular layer (2.4 nm thick) that is smaller than a neuron synapse (~1–10 μm) by at least three orders of magnitude, and thinner even than the synaptic gap (~20–40 nm) by an order of magnitude. This dynamic nature represents a new class of multifunctional molecular switch that simplifies brain-inspired electronic devices, and opens the door to neuromorphic computing at the molecular scale.

One of the goals of neuromorphic electronics is to produce computing systems in which the training is done at the hardware level, but the molecular hardware for doing so is not available. Unlike the molecular switches studied so far, biological switches, which include synapses, are inherently dynamic as they operate far away from thermodynamic equilibrium[13,14] and therefore can be trained. In synapses (Fig. 1a), information travels in the form of an action potential from a presynaptic neuron to a postsynaptic neuron through the synaptic gap, as regulated by the combined excitatory and inhibitory neural inputs[15]. By coupling different processes each characterized with different time constants, here fast depolarization coupled to the slow diffusion of Ca^{2+} and neurotransmitters, the synapses can be strengthened or weakened depending on their activity[16], which results in a synaptic plasticity that enables pulse-pair facilitation (PPF) and depression (PPD) with a spike-rate and timing-dependent plasticity. To emulate the dynamic behaviour of synapses at the molecular level, we combined the fast electron transfer (akin to action potentials and fast depolarization processes) with a slow proton coupling limited by diffusion (akin to the role of Ca^{2+} or neurotransmitters).

Solid-state dynamic molecular switches

Figure 1b–d shows the DMS we introduce here, incorporated in junctions that consist of a self-assembled monolayer (SAM) supported by a gold bottom electrode in contact with an EGaIn top electrode. The SAM molecule has a 5,6,11,12,17,18-hexaazatrinaphthylene (HATNA) terminus that readily undergoes six successive proton coupled electron transfer (PCET) steps for dynamic covalent N–H bond formation[17,18]. In the following we indicate the various oxidation states as H_n-HATNA with $n = 0–6$. When the molecules were reduced ($n = 0–2$) and turned on, electron transfer (ET) across the junctions was fast (fast channel, indicated by the blue arrow in Fig. 1c), which resulted in a large increase in the currents that flowed across the junction. In parallel to this fast ET process, proton addition steps occurred and N–H formation slowed down the ET rate (slow channel, dashed blue arrow in Fig. 1d) and turned the junction off as HATNA was progressively reduced ($n = 3–6$). In our experiments, water from the ambient (air at room temperature) was the proton source and the proton transfer (PT) was diffusion limited and much slower than the ET. This switching from the fast to slow channel occurred at a negative bias when the molecules were reduced, which resulted in a decrease of the current and a negative differential resistance (NDR). The junctions were oxidized back to their original states by applying a positive bias. As the ET and PT steps occurred at very different timescales, our junctions can emulate the plastic behaviour of synapses, Pavlovian learning and all logic gates, simply by changing the applied voltage and the duration of voltage pulses.

PCET and dynamic covalent bond formation

We characterized the structure of the SAMs using various techniques (Methods and Supplementary Sections 2 and 3) and concluded that the SAMs were densely packed with all the HATNA units confined to

the top of the SAM, as shown, for instance, by the molecular dynamics simulations (Fig. 2a–c). To prove that the SAMs underwent sequential PCET via stable intermediates for a reliable switching, we recorded a cyclic voltammogram (CV) from a S-C_{10}-HATNA SAM (Fig. 2d) in which four distinct redox waves are visible, similar to the results of Ohsaka and co-workers[18] (Supplementary Section 3.1). They proposed that protonation initiates the first PCET step followed by the ring-by-ring reduction of HATNA (Fig. 2e), which explains why the PCET cascade appears as distinct redox waves. Our density functional theory (DFT) calculations confirm this mechanism (Supplementary Section 4).

Although the fully reduced SAM has essentially the same supramolecular structure as the SAM in its initial state (Fig. 2c), our DFT calculations revealed that the electronic structure of the SAM strongly depends on the oxidation and protonation state of HATNA. Figure 2f shows the projected density of states (PDOS) of the molecule during PCET following the steps in Fig. 2g calculated with DFT. Figure 2g shows that the molecule in the initial state (H_0-HATNA) has a large HOMO–LUMO gap (HOMO, highest occupied molecular orbital; LUMO, lowest unoccupied molecular orbital) of 2.1 eV, but on the initial protonation that results in (HATNA)H^+, a new mid-gap state appears at around 1.1 eV above the Fermi energy (E_F) of the Au electrode, which provides a low-energy tunnelling channel that defines the on state of the junction (Fig. 1b and see Fig. 4 below). This state persists during the first two PCET steps and results in H_n-HATNA with $n = 1$ and 2 (Fig. 1c) but then shifts towards a lower energy before disappearing for H_5-HATNA, and the large conductance gap is restored (Fig. 1d and see Fig. 4 below), which turns the junction off to give a NDR, as explained below. The changes in HOMO, LUMO, and the mid-gap energy levels during all the proton and electron addition steps are given in Fig. 2g, Extended Data Fig. 1 and Supplementary Section 4.

Hysteretic negative differential conductance

Figure 3 shows the J(V) response from the Au-S-C_{10}-HATNA//Ga_2O_3/EGaIn junctions (see Methods for details). The large hysteretic NDR peak can be explained by following the applied voltage in steps (1) → (4) as indicated, where HATNA continuously changes its redox state (indicated by the top axis). Step (1): the voltage was increased to +1.0 V, which ensured the HATNA moieties were oxidized ($n = 0$, Fig. 4a). Step (2): the voltage was reduced and at around −0.9 V the current sharply increased as an empty molecular state entered the bias window and the mechanism of charge transport changed the resonant tunnelling from off to on (Fig. 4b,c). The PDOS data indicate that the lowest available tunnelling level was the mid-gap state associated with (HATNA)H^+, which is likely given the basic nature of HATNA (and confirmed with vibrational sum-frequency generation spectroscopy described in Supplementary Section 3.3). Step (3): with an increasing negative bias, the junctions progressively turned on to form H_n-HATNA with $n = 1$ and 2 (which have this mid-gap state), but turned off at a large negative bias when the molecules were reduced to give H_n-HATNA with n = 5 and 6 (which lack the mid-gap state), which results in a reduction of the current (Fig. 4e,f) and consequential NDR. Step (4): during the retrace from −2 to 0 V, junctions remained in the off state (Fig. 4d), which resulted in a large hysteretic NDR with a memory. Only at a positive bias were the H_n-HATNA moieties oxidized to HATNA ($n = 0$) when the HOMO fell inside the conduction window and the cycle restarted (reset from Fig. 4d to Fig. 4a). The value of R_{PtV} (the current ratio between the peak and the valley for the NDR effect) was 13.7 ± 3.5 (at 10 mV s^{-1}) and the value of $R_{on/off}$ (current ratio between the forward peak current and reverse current at the same voltage) was 2.64 ± 1.41 × 10^2, which are among the highest values recorded in molecular junctions[19].

Theoretical model for NDR and dynamic switches

There are currently no ab initio theories available that can model the dynamical behaviour of junctions, but the analytical model developed by Migliore and Nitzan[20] captures all our observations, as illustrated
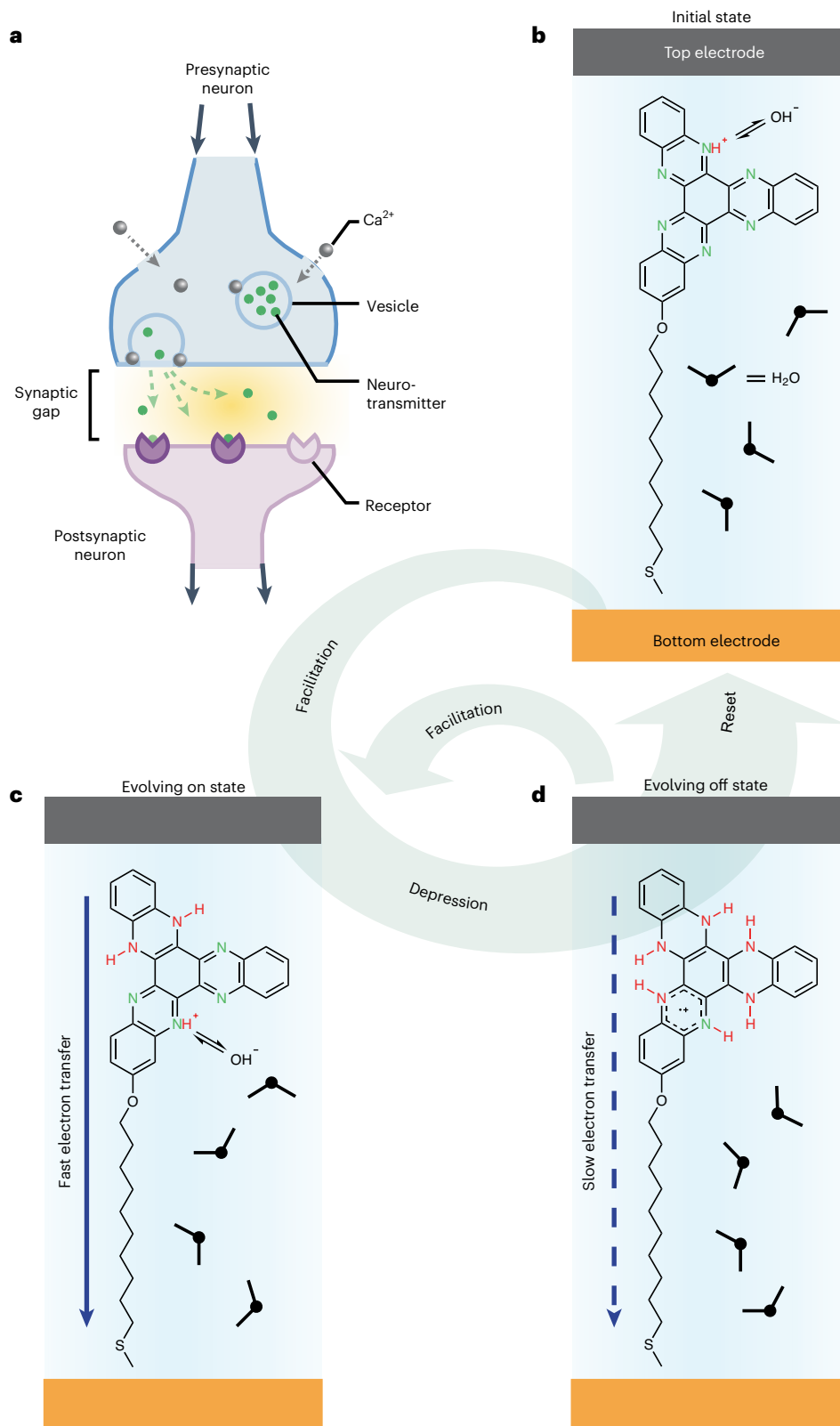
Fig. 1 | The dynamic molecular junction. a–d, Schematic of a synapse (**a**) and the junctions (**b–d**). **b,** The junction consists of a Au bottom electrode and an EGaIn top electrode (EGaIn, eutectic alloy of gallium and indium). **c,d,** Solid and dashed blue arrows indicate electron transfer (ET) via coherent tunnelling through the fast (**c**) and slow (**d**) channels. The two ET channels are bridged by slow PCET in which the protons are provided by water molecules in the air.

in Fig. 4 in the form of energy-level diagrams constructed on the basis of our DFT (Fig. 2f,g) and spectroscopy results (Supplementary Section 3.2). The model helps us to identify the switching regimes in

detail (as demonstrated previously for other switches[21]) and, more importantly, establishes the mechanism of the time- and applied-voltage dependency of the dynamical behaviour of the switching. The model
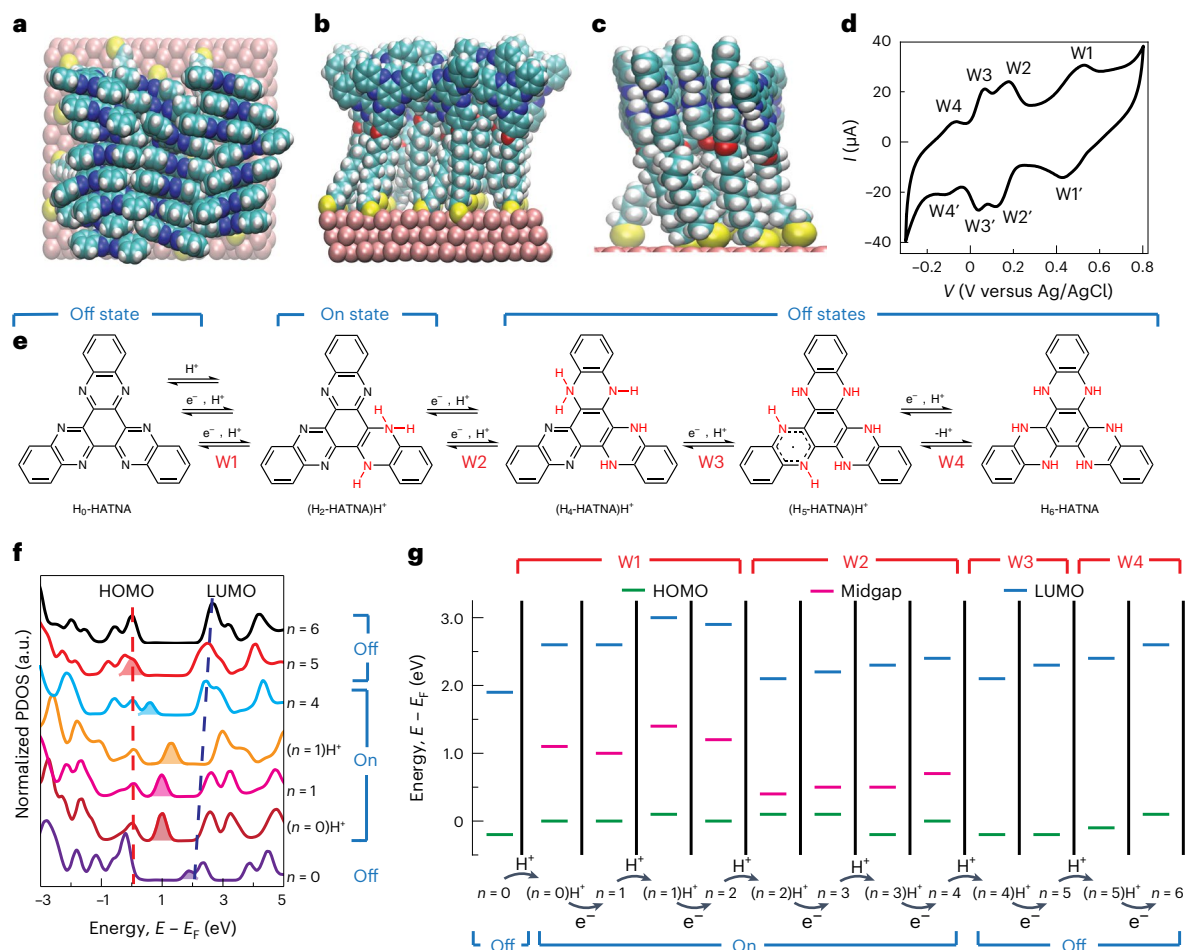
Fig. 2 | Mechanism of PCET. a–c, Representative computed structures of π–π-driven supramolecular packing in S-C_{10}-HATNA SAMs on Au(111), from 0.1 ms of equilibrated room temperature molecular dynamics with H_0-HATNA shown from above (**a**) and from the side (**b**), and a zoom-in on H_6-HATNA shown from the side (**c**). Carbon, cyan; nitrogen, navy; oxygen, red; sulfur, yellow; hydrogen, white. **d**, CV of a HATNA SAM on Au in contact with 2.0 M aqueous $HClO_4$ recorded at a scan rate of 0.5 V s^{-1} (W1–W4 and W1′–W4′ represent the four redox waves of the HATNA SAM). **e**, Proposed PCET mechanism. **f,g**, Calculated PDOS on the molecule of HATNA SAMs on Au(111) for selected oxidation and protonation states (see Extended Data Fig. 1 for all the states) (**f**) and the corresponding HOMO, LUMO and mid-gap energy levels for all the states (**g**). The oxidation state is indicated by n and the protonation states are indicated by H$^+$ (Supplementary Fig. 14). a.u., arbitrary units.

describes simultaneous fast ET and slow PT processes in a molecular junction that lead to switching between fast and slow ET channels (Fig. 1), as described in detail in Supplementary Section 6. No molecular orbitals are available for charge transport at a low bias, but at an intermediate negative bias (step (3) in Fig. 3a) the mid-gap state enters the conduction window, which increases the ET rates of the on state (R_{AB} and R_{BA}, as shown in Fig. 4b,c) after the addition of one H$^+$, that is, H_0-HATNA → (H_0-HATNA)H$^+$. This protonation step changes the tunnelling barrier height defined by the LUMO to that defined by the mid-gap state, as indicated by χ (Fig. 4e,f) and the molecule–electrode coupling strength (given by γ and factor κ). Thus, χ defines the mid-gap in the LUMO energy difference, which is 2.1 eV (Supplementary Section 6) in good agreement with DFT (1.5–2.0 eV, Fig. 2g). At a high bias, the HATNA moieties are progressively reduced and junctions turn off again, which lowers the ET rates $R_{\overline{AB}}$ and $R_{\overline{BA}}$ (defined in Fig. 4e,f) and results in NDR. In parallel, PT (R_{+PC} and R_{-PC}) occurs at much slower rates than ET across both the fast and slow channels (that is, $R_{+PC} \ll R_{AB}, R_{\overline{AB}}$), but PT is responsible for switching. Therefore, the ET rates (R_{AB}, R_{BA} and $R_{\overline{AB}}, R_{\overline{BA}}$) and associated currents in the on (I^{AB}) and off ($I^{\overline{AB}}$) state are modelled with a single-level Landauer model[22], whereas the much slower PT steps (R_{-PC}, R_{+PC}) are described by Marcus

theory, which is routinely used to model PCET steps[23–25]. Following Migliore and Nitzan's model[20], the current that flows across the junctions is calculated from the probability of the junctions to be in the on (P^{AB}) or off ($P^{\overline{AB}}$) state as given by:

$$I(V) = P^{AB}(V)I^{AB}(V) + P^{\overline{AB}}(V)I^{\overline{AB}}(V) \qquad (1)$$

where $P^{AB}(V) = 1 - P^{\overline{AB}}(V)$. The overall dynamical probability of the junction is governed by the slow protonation rates $< R_{+PC} >$ and $< R_{-PC} >$

$$\frac{dP^{AB}}{dt} = (1 - P^{AB}) < R_{+PC} > -P^{AB} < R_{-PC} > \qquad (2)$$

Figure 3c shows a fit of this model to the $J(V)$ data and reproduces all the important observations: NDR, hysteretic switching and the reset at a positive bias (which involves the HOMO, Fig. 4a,d and Supplementary Section 6). This modelling of the junction successfully describes the behaviour, as shown in Fig. 3c, and confirms that the appearance and disappearance of the mid-gap state causes switching and gives feedback on how and when the protonation occurs by giving
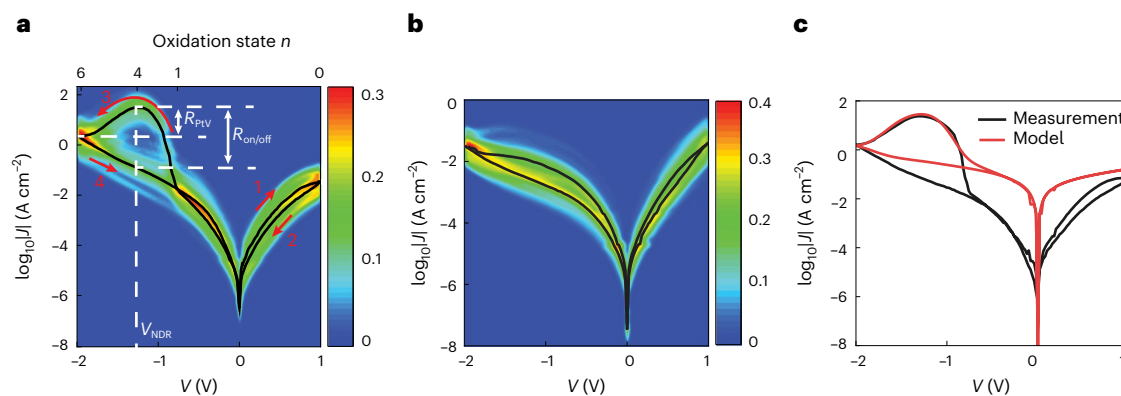
Fig. 3 | Electrical characteristics of the Au-S-C$_{10}$-HATNA//Ga$_2$O$_3$/EGaIn junctions. a,b, Heatmap of log$_{10}$|J| versus V (24 °C, relative humidity = 60% in ambient conditions) (**a**) and heatmap of log$_{10}$|J| versus V measured (**b**) under an atmosphere of compressed air with 10 ppm water. The black line is the log-median average curve (<log$_{10}$|J|>$_m$ versus V). **c,** Representative dataset with a fit to the theoretical model (fitting parameters given in Supplementary Table 15). The red arrows (1), (2), (3) and (4) in **a** represent the applied voltage in four steps as discussed in the main text. V_{NDR}, the voltage of the NDR peak.
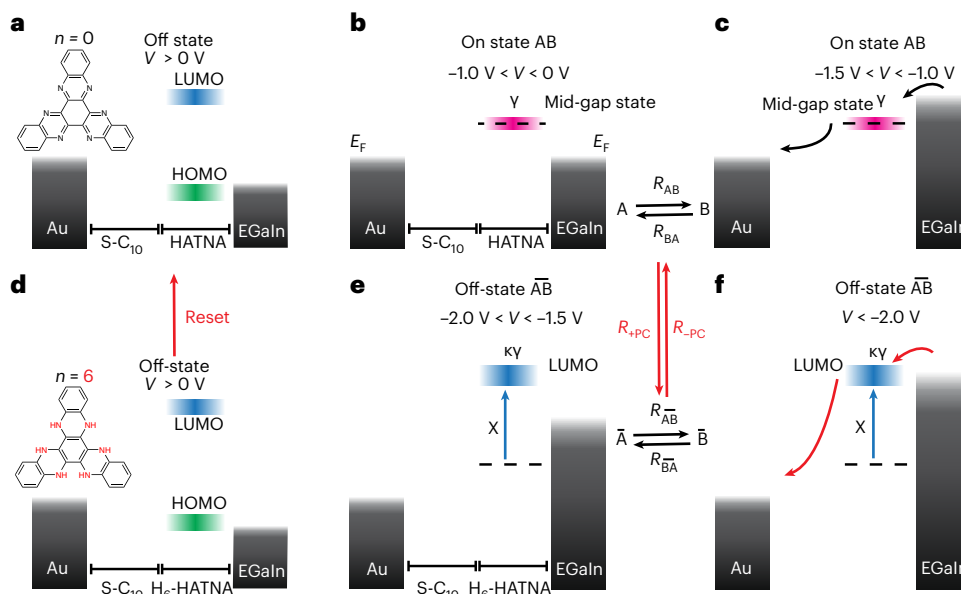
Fig. 4 | Model of the dynamic switch. a–f, Energy level diagrams of the off (**a,d–f**) and on (**b,c**) states of the junctions at which tunnelling is mediated by the acceptor level lying above the E_F (blue bar), which is the LUMO at a low negative or positive bias (**a,b**) when off-resonant tunnelling dominates but falls in the conduction window at an elevated negative bias when the low-lying mid-gap state forms because of PCET (**c**). The rate equations describe coherent ET tunnelling (horizontal transitions) coupled to slow PT steps (vertical transitions). H$_6$-HATNA can be reset into H$_0$-HATNA by applying a positive V (**d**). PT increases the tunnelling barrier height of the ET channel by an interaction energy χ which decreases the molecule–electrode coupling strength γ by a factor κ (resulting in a broad LUMO) (**e**), which results in NDR. The LUMO in the off state is energetically accessible only at a large negative bias (**f**). Note: although the DFT calculations in Fig. 2f,g suggest that the HOMO level is close in energy to the E_F, the ultraviolet photoelectron spectroscopy data indicate that the HOMO level is 2.1 eV below the E_F of the Au electrode (Supplementary Section 3.2). Given the common problem of level alignment in DFT calculations[40], we relied on the ultraviolet photoelectron spectroscopy in **a–f**.

an estimate for the switching probability. To demonstrate that the presence of water is important, we repeated the experiment with relative humidity <5%, and no NDR effect was found (Fig. 3b).

Emulating synaptic behaviour

To demonstrate the basic synaptic function with our junctions, we performed PPF and PPD as follows. Figure 5a shows a typical pulse-pair sequence and current response. The difference in chordal conductance ($G = I_{bias}/V$) between the measured and reference pulse in the pair, divided by the chordal conductance of the reference pulse, $\Delta G/G$, was used to quantify PPF and PPD, along with a modelled current response

(more detail given in Supplementary Section 5.2). The magnitudes of the voltage pulse (V_p), pulse duration (t_p) and time delay between consecutive pulses (t_d) programme the junction. For instance, Fig. 5b shows that by changing V_p (with $t_p = t_d = 1$ s) both conductance enhancement (excitatory potentiation) and depression (inhibitory potentiation) are obtained (Extended Data Fig. 2). Figure 5c shows that the extent of the potentiation depends on t_p where $\Delta G/G$ follows an exponential decay with a characteristic time of 2.4 ± 0.9 s (Extended Data Fig. 3 and Supplementary Section 5.2.1.2).

Changing the delay between pulses provided different programming schemes. No substantial decay was found in delays over minutes
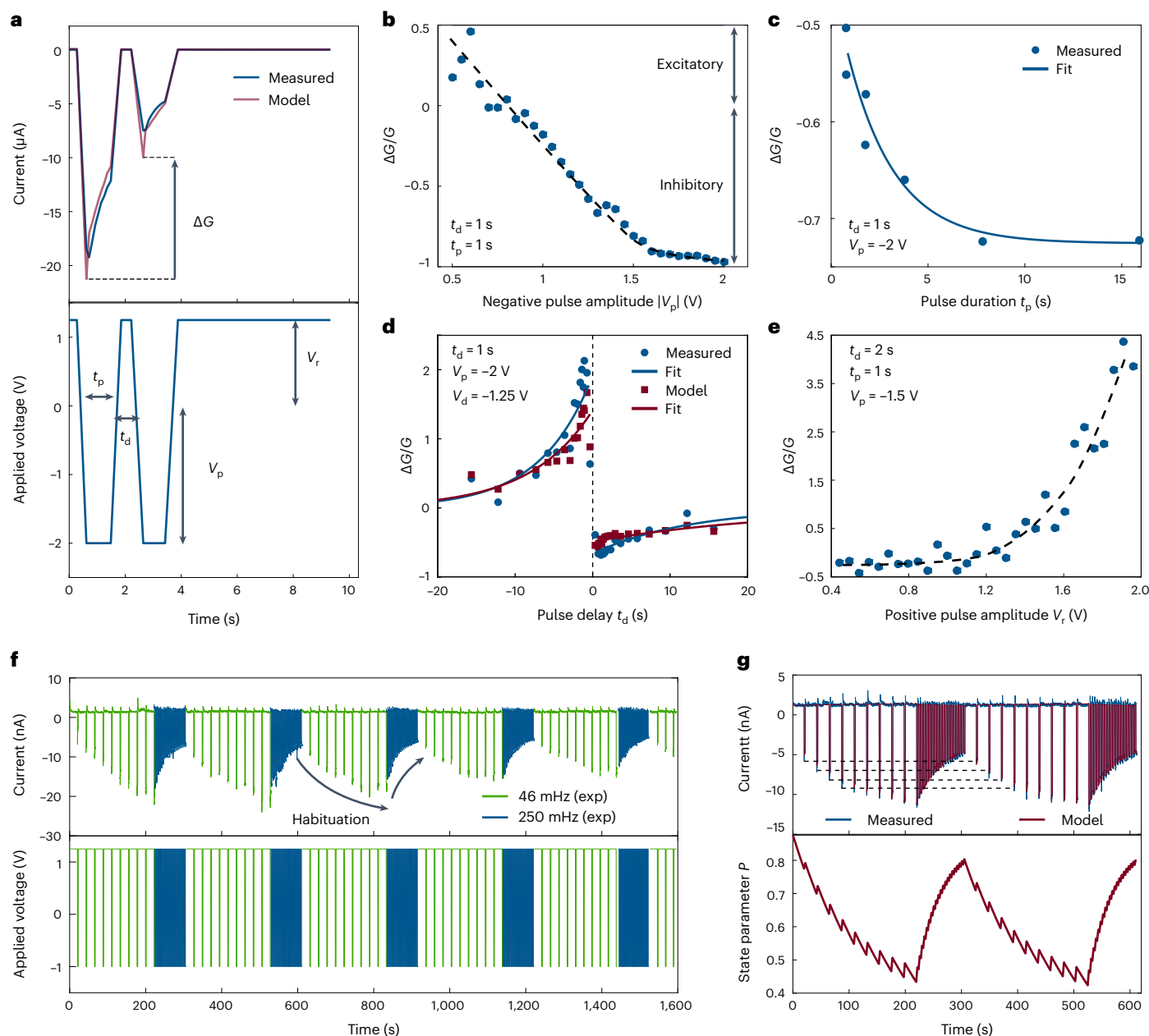
Fig. 5 | Synaptic function. a, Typical voltage paired-pulse sequence and current response used to extract PPF and PPD properties, as measured (blue line) and modelled (red line) (additional fits are given in Supplementary Section 6.3). ΔG is the difference in chordal conductance between the measured and reference pulse as indicated by the arrow. **b**–**e**, The relative potentiation (change in the static conductance relative to the conductance of the reference pulse) $\Delta G/G$ measured as a function of: negative V_p amplitude (**b**), t_p (**c**), interpulse delay (t_d) (**d**) and positive pulse amplitude (V_r) (**e**). Blue dots, measured data; red squares, data obtained from the model; dashed black lines (**b**,**e**), visual guides; solid blue lines (**c**,**d**), exponential fits used to extract the characteristic time constants (Supplementary Sections 5.2.1.2 and 6.3). The pulse sequences and $I(V)$ profiles of the junctions used are shown in Extended Data Figs. 2–5. **f**, Pulse sequence exhibiting spike-rate-dependent plasticity with $V_p = -1$ V at 46 mHz or 250 mHz and an interpulse delay at $V_d = 1.25$ V. The solid black arrows indicate the effects of habituation. **g**, Identification and retrieval of conductance states over successive cycles and fit to the model. Dashed black lines are visual guides to show the recovery of the first four conductance states. The lower panel shows the evolution of dynamical switching probability P. exp, experimental.

if the voltage was set at 0 V (Supplementary Section 5.2.1.3). However, the delay voltage can be set to a positive value, that is, reset voltage V_r, so that the junction resets over time. Figure 5d shows that by changing t_d (with $V_p = -2.0$ V and $t_p = 1$ s), the conductance decreases exponentially with a characteristic time of ~2.5 s (Extended Data Fig. 4 and Supplementary Section 5.2.1.2). The speed of this reset process can be adjusted through the magnitude of V_r (Fig. 5e and Extended Data Fig. 5). Figure 5d shows that spike-timing-dependent plasticity, where the order in which the pulses are applied and the delay between

them modulates $\Delta G/G$, can also be emulated (Supplementary Section 5.2.1.2). The characteristic decay times of 12 s for positive t_p and 7 s for negative t_p are consistent with values obtained from our model (24 s and 8 s respectively). Spike rate dependent plasticity is shown in Fig. 5f. A negative inhibitory pulse ($V_p = -1.0$ V, $t_p = 2$ s) was applied at a set rate while a positive excitatory voltage ($V_d = 1.25$ V) was sustained during the delay between these pulses. Depending on the rate of the inhibitory pulse, the junction can have a net excitatory (46 mHz) or inhibitory (250 mHz) evolution over successive periods. These results
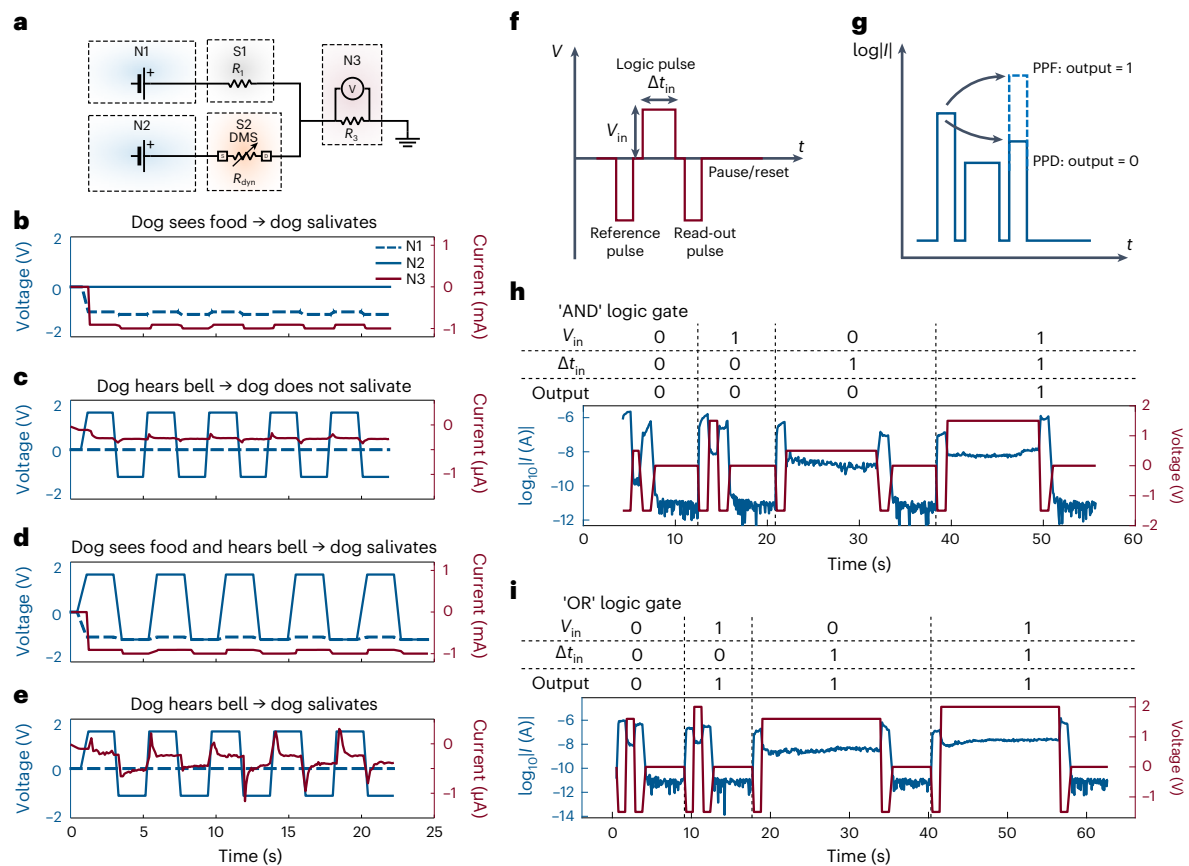
Fig. 6 | Demonstration of Pavlovian learning and Boolean logic gates using time plasticity in the DMS. a, Schematic of the electrical circuit. Two input neurons N1 and N2 are connected to an output neuron N3 via synapses S1 (resistor), which enables a strong coupling between N1 and N3, and S2 (DMS), the trainable synapse. **b**–**e**, Pulse sequences showing Pavlovian learning. **b**, Pulse sequence representing 'dog sees food', pulses from N1 produce a strong output in N3. **c**, 'Dog hears bell' before training, N2 produces an insignificant output in N3. **d**, 'Dog sees food and hears bell', which trains S2. Pulses from N1 and N2 combined

produce a strong output in N3. **e**, 'Dog hears bell' after training, N2 now produces a substantial output in N3. **f**, A reference voltage pulse is followed by the logic pulse to perform the operation and finally a read-out pulse. **g**, The current read-out pulse is compared to the reference pulse, where current increase is defined as output = 1 and current decrease as output = 0. Demonstration of the AND (**h**) and OR (**i**) logic gates. All other gates and input parameters are shown in Extended Data Fig. 8 and Supplementary Section 5.2.3.

demonstrate that, as in biological neural systems[26,27], the frequency of the signal decides the (synaptic) junction response. This rate control provides a way to create discrete conductance states that can be recognized in subsequent cycles using several regular pulses. Figure 5g shows that junctions successfully reproduced discretization of ten conductance states; this behaviour could be fully modelled. Repeated identical pulses did not potentiate the junction in a constant manner; instead, the junctions showed habituation, that is, the junction desensitized to the signal as the response decayed exponentially (as indicated in Fig. 5f), which mimics how biological systems avoid overstimulation[28]. This habituation can be reversed through reset pulses and can be explained by the finite number of molecules electrically active in the junction, as captured by the model. Extended Data Fig. 6 shows that the junctions are stable against voltage cycling (we tested the stability for 10^5 cycles of −2 to +1 V; see Supplementary Section 5.3 for additional information) and can operate at higher speeds (millisecond range; see Supplementary Section 7 for additional discussion), similar to that of electrochemical synaptic devices[1–3,7,29].

Emulating Pavlovian learning and logic gates

Figure 6 shows a system that mimics Pavlov's experiment that demonstrated the potential for the synapse to serve as a basis for Hebbian learning, that is, the training of an input by the simultaneous operation with another input ('neurons that fire together, wire together'[15]).

Two inputs were fired from neurons N1 and N2 (here sources of voltage pulses) through synapses (electronic junctions) S1 and S2, respectively, to output neuron N3 (an ammeter), as shown in Fig. 6a. In the Pavlov analogy, N1 represents 'dog sees food' which readily delivers an output in N3 'dog salivates' (Fig. 6b). The sensitized synapse S1 between the two was materialized by a low-resistance resistor in the circuit. However, N2 (or 'dog hears bell') does not readily deliver the output in N3 (see the unsubstantial output in Fig. 6c, 'dog does not salivate'), but can be trained to do so through the simultaneous operation of N1 and N2 (Fig. 6d, 'dog sees food and hears bell'). This sensitizes the adaptive synapse S2 (the dynamic switch) and subsequently enables N2 to produce an output in N3 (Fig. 6e) (Extended Data Fig. 7). In this set-up, the whole Hebbian learning functionality is provided by the DMS, without the use of a third terminal and additional relays, as reported before[29].

Components that can perform logic can be used as hidden layers in hardware deep-learning systems[30]. The time-domain plasticity of the DMS can be used to emulate all standard Boolean logic gates. Although the DMS is a two-terminal component and standard logic gates require at least two inputs for one output, the time-domain plasticity of the DMS makes it possible to consider an applied voltage pulse as two separate inputs by separating the voltage and time domains in the pulse. The voltage magnitude of the pulse is one input and its duration a second input, and the resulting modulation in the conductance of the

junction represents the output: positive if excitatory, and negative if inhibitory (Fig. 6f,g). By defining the input states V_{on}, V_{off}, t_{on} and t_{off}, the DMS can provide all the fundamental logic gates, as shown in Fig. 6h,i and Extended Data Fig. 8 (Supplementary Section 5.2.3).

Outlook

We report a DMS of just 2.4 nm that readily emulates the plasticity of synapses, exhibits Pavlovian learning and can be configured to perform all the logic gates required for deep learning, all within one junction. This multifunctionality combined with reconfigurability has the potential to considerably simplify brain-inspired electronic devices. The switching probability of the junction changes dynamically between high and low conduction states enabled via PCET-driven dynamic N–H bond formation. A challenge is usually to understand the microscopic origin of the dynamics of mesoscale artificial synapses, and such systems are usually modelled with equivalent circuit analysis or network models. In contrast, the dynamical behaviour of our DMS can be readily captured with intertwined rate equations with different time constants and can be applied to dynamic molecular systems driven by other stimuli (such as light[31]) and coupled to different types of dynamic covalent bond formation[32], which open up a whole new range of adaptive and reconfigurable systems with orthogonal inputs and outputs. In principle, the reaction dynamics of the DMS can be controlled via the proton source (for example, by changing the relative humidity or incorporating proton sources in the monolayer) or by changing to other types of dynamic covalent bonds[33,34], which leads to interesting ways to control the dynamical properties of molecular devices. On a final note, it is well-known that redox-active groups, mobile ions or water alone in molecular junctions can induce electronic function, such as non-volatile memory or rectification[35–39]; they do not result in the type of plasticity reported here (Supplementary Section 9). Our results demonstrate that PCET is a promising way to induce plasticity in molecular junctions and opens up a new way to design junctions that emulate brain-like features.

Online content

Any methods, additional references, Nature Research reporting summaries, source data, extended data, supplementary information, acknowledgements, peer review information; details of author contributions and competing interests; and statements of data and code availability are available at https://doi.org/10.1038/s41563-022-01402-2.

References

1. Van De Burgt, Y., Melianas, A., Keene, S. T., Malliaras, G. & Salleo, A. Organic electronics for neuromorphic computing. *Nat. Electron.* **1**, 386–397 (2018).
2. Zhu, J., Zhang, T., Yang, Y. & Huang, R. A comprehensive review on emerging artificial neuromorphic devices. *Appl. Phys. Rev.* **7**, 011312 (2020).
3. Upadhyay, N. K. et al. Emerging memory devices for neuromorphic computing. *Adv. Mater. Technol.* **4**, 1800589 (2019).
4. Chen, T. et al. Classification with a disordered dopant-atom network in silicon. *Nature* **577**, 341–345 (2020).
5. Keene, S. T. et al. A biohybrid synapse with neurotransmitter-mediated plasticity. *Nat. Mater.* **19**, 969–973 (2020).
6. Oh, S., Hwang, H. & Yoo, I. K. Ferroelectric materials for neuromorphic computing. *APL Mater.* **7**, 91109 (2019).
7. Wang, L., Lu, S. R. & Wen, J. Recent advances on neuromorphic systems using phase-change materials. *Nanoscale Res. Lett.* **12**, 1–22 (2017).
8. Wan, Q., Sharbati, M. T., Erickson, J. R., Du, Y. & Xiong, F. Emerging artificial synaptic devices for neuromorphic computing. *Adv. Mater. Technol.* **4**, 1900037 (2019).
9. Xu, W., Min, S. Y., Hwang, H. & Lee, T. W. Organic core–sheath nanowire artificial synapses with femtojoule energy consumption. *Sci. Adv.* **2**, e1501326 (2016).
10. Ratera, I. & Veciana, J. Playing with organic radicals as building blocks for functional molecular materials. *Chem. Soc. Rev.* **41**, 303–349 (2012).
11. Klajn, R. Spiropyran-based dynamic materials. *Chem. Soc. Rev.* **43**, 148–184 (2014).
12. Bléger, D. & Hecht, S. Visible-light-activated molecular switches. *Angew. Chem. Int. Ed.* **54**, 11338–11349 (2015).
13. Sorrenti, A., Leira-Iglesias, J., Markvoort, A. J., De Greef, T. F. A. & Hermans, T. M. Non-equilibrium supramolecular polymerization. *Chem. Soc. Rev.* **46**, 5476–5490 (2017).
14. Van Rossum, S. A. P., Tena-Solsona, M., Van Esch, J. H., Eelkema, R. & Boekhoven, J. Dissipative out-of-equilibrium assembly of man-made supramolecular materials. *Chem. Soc. Rev.* **46**, 5519–5535 (2017).
15. Bear, M. F., Connors, B. W. & Paradiso, M. A. *Neuroscience: Exploring the Brain* (Wolters Kluwer, 2016).
16. Eccles, J. C. & McIntyre, A. K. Plasticity of mammalian monosynaptic reflexes. *Nature* **167**, 466–468 (1951).
17. Segura, J. L., Juárez, R., Ramos, M. & Seoane, C. Hexaazatriphenylene (HAT) derivatives: from synthesis to molecular design, self-organization and device applications. *Chem. Soc. Rev.* **44**, 6850–6885 (2015).
18. Wang, R. et al. Cyclic and normal pulse voltammetric studies of 2,3,6,7,10,11-hexaphenylhexazatriphenylene using a benzonitrile thin layer-coated glassy carbon electrode. *J. Phys. Chem. B* **107**, 9452–9458 (2003).
19. Perrin, M. L. et al. Large negative differential conductance in single-molecule break junctions. *Nat. Nanotechnol.* **9**, 830–834 (2014).
20. Migliore, A. & Nitzan, A. Irreversibility and hysteresis in redox molecular conduction junctions. *J. Am. Chem. Soc.* **135**, 9420–9432 (2013).
21. Schwarz, F. et al. Field-induced conductance switching by charge-state alternation in organometallic single-molecule junctions. *Nat. Nanotechnol.* **11**, 170–176 (2016).
22. Garrigues, A. R. et al. A single-level tunnel model to account for electrical transport through single molecule- and self-assembled monolayer-based junctions. *Sci. Rep.* **6**, 26517 (2016).
23. Warren, J. J. & Mayer, J. M. in *Proton-Coupled Electron Transfer: A Carrefour of Chemical Reactivity Traditions* (eds Formosinho, S. & Barroso, M.) 1–31 (The Royal Society of Chemistry, 2012).
24. Migliore, A., Polizzi, N. F., Therien, M. J. & Beratan, D. N. Biochemistry and theory of proton-coupled electron transfer. *Chem. Rev.* **114**, 3381–3465 (2014).
25. Mayer, J. M. Understanding hydrogen atom transfer: from bond strengths to Marcus theory. *Acc. Chem. Res.* **44**, 36–46 (2011).
26. Kim, S. et al. Experimental demonstration of a second-order memristor and its ability to biorealistically implement synaptic plasticity. *Nano Lett.* **15**, 2203–2211 (2015).
27. Wang, Z. et al. Memristors with diffusive dynamics as synaptic emulators for neuromorphic computing. *Nat. Mater.* **16**, 101–108 (2017).
28. Thompson, R. in *International Encyclopedia of the Social & Behavioral Sciences* (eds Smelser, N. J. & Baltes, P. B.) 6458–6462 (Pergamon, 2001).
29. Van De Burgt, Y. et al. A non-volatile organic electrochemical device as a low-voltage artificial synapse for neuromorphic computing. *Nat. Mater.* **16**, 414–418 (2017).
30. Ruiz Euler, H. C. et al. A deep-learning approach to realizing functionality in nanoelectronic devices. *Nat. Nanotechnol.* **15**, 992–998 (2020).

31. Kathan, M. et al. Light-driven molecular trap enables bidirectional manipulation of dynamic covalent systems. *Nat. Chem.* **10**, 1031–1036 (2018).

32. Chakma, P. & Konkolewicz, D. Dynamic covalent bonds in polymeric materials. *Angew. Chem. Int. Ed.* **58**, 9682–9695 (2019).

33. Cafferty, B. J. et al. Robustness, entrainment, and hybridization in dissipative molecular networks, and the origin of life. *J. Am. Chem. Soc.* **141**, 8289–8295 (2019).

34. Ashkenasy, G., Hermans, T. M., Otto, S. & Taylor, A. F. Systems chemistry. *Chem. Soc. Rev.* **46**, 2543–2554 (2017).

35. Shi, J. et al. The influence of water on the charge transport through self-assembled monolayers junctions fabricated by EGaIn technique. *Electrochim. Acta* **398**, 139304 (2021).

36. Ai, Y. et al. In-place modulation of rectification in tunneling junctions comprising self-assembled monolayers. *Nano Lett.* **18**, 7552–7559 (2018).

37. Barber, J. R. et al. Influence of environment on the measurement of rates of charge transport across Ag^{TS}/SAM//Ga$_2$O$_3$/EGaIn junctions. *Chem. Mater.* **26**, 3938–3947 (2014).

38. Han, Y. & Nijhuis, C. A. Functional redox-active molecular tunnel junctions. *Chem. Asian J.* **15**, 3752–3770 (2020).

39. Han, Y. et al. Electric-field-driven dual-functional molecular switches in tunnel junctions. *Nat. Mater.* **19**, 843–848 (2020).

40. Egger, D. A., Liu, Z. F., Neaton, J. B. & Kronik, L. Reliable energy level alignment at physisorbed molecule–metal interfaces from density functional theory. *Nano Lett.* **15**, 2448–2455 (2015).

Methods

Synthesis

HATNA was synthesized following a similar procedure to that reported previously[41]; the detailed synthesis scheme and characterization of the molecule are summarized in Supplementary Section 2.

Electrode preparation

The cone-shaped GaO_x/EGaIn top electrode was formed using previously reported methods[42]. The gold bottom electrode was prepared following reported template stripping methods[43]. We deposited 200-nm-thick Au films (which contained 99.999% Au granules, ACI Alloys) on commercial Si(100) wafers (with a native SiO_2 thin layer on the surface) using a Shen Yang Ke Yi thermal evaporator. Clean glass slides were then glued onto the Au surface with thermal glue (EPOTEK 353ND) and cured at 80 °C for 3 h. To minimize contamination from the atmosphere, the wafers coated with Au were stored in a dry box and the Au was template-stripped (Au^{TS}) immediately before use.

Self-assembled monolayer formation on Au^{TS}

The S-C_{10}-HATNA SAMs were formed using well-established methods[42]. Typically, 1.0 mg of HS-C_{10}-HATNA was dissolved in freshly distilled tetrahydrofuran (6 ml) to obtain a solution with a concentration of 0.2–0.3 mM. The solution was degassed for 15 min with N_2 to remove oxygen, and then fresh Au^{TS} surface was immersed into the solution for 24 h under an atmosphere of N_2. The coated Au substrates were then removed from the solution and washed with tetrahydrofuran and ethanol to remove physisorbed molecules and gently dried in a flow of N_2.

Electrochemistry

The S-C_{10}-HATNA SAMs on Au were electrochemically characterized by cyclic voltammetry. We used a custom-built electrochemical cell equipped with a Pt counter electrode, Ag/AgCl reference electrode and Au^{TS} working electrode. A $HClO_4$ aqueous solution (2 M) was used as the electrolyte, similar to that previously reported[18]. The CVs were recorded between −0.3 and 0.8 V at scan rates that ranged from 0.05 to 10 V s^{-1} with an Autolab PGSTAT302T equipped with NOVA 1.10 software (Supplementary Section 3).

Surface characterization

Synchrotron-based photoemission spectroscopy, including X-ray photoelectron spectroscopy (XPS), ultraviolet photoelectron spectroscopy and near-edge X-ray absorption fine structure spectroscopy were performed using the Surface, Interface and Nanostructure Science beamline of the Singapore Synchrotron Light Source. The experimental procedures are described in our previous work[44]. We measured the SAMs of S-C_{10}-HATNA on Au^{TS} surfaces. For high-resolution XPS, we used photon energies of 350 eV for S 2p and C 1s, 600 eV for N 1s and 650 eV for O 1s spectra for the optimal photoionization cross-sections at these core levels. We recorded each XPS signal with two different photoelectron take-off angles, 90° (normal emission) and 40° (grazing emission). We performed peak fitting using pseudo-Voigt functions with a fixed 70% Gaussian and 30% Lorentzian ratio and a Shirley background. The detailed results of the surface characterization are shown in Supplementary Section 3.

DFT electronic structure calculations

We calculated the density of states distributions for the HS-C_{10}-HATNA and the reduced state HS-C_{10}-(H_6-HATNA) and for all the intermediate states along the PCET path using previously reported methods[40]. All the computed reorganization energies of HATNA during the sequential PCET steps, the calculated PDOS of Au-S-C_{10}-HATNA and post-PCET Au-S-C_{10}-(H_6-HATNA), the computed surfaces of the electron acceptor mid-gap and LUMO → LUMO+2 levels, and the calculated PDOS on the molecule of HATNA SAMs on Au(111) for all the intermediate oxidation and protonated states are summarized in Supplementary Section 4.

Junction fabrication and electrical measurements in air

We formed electrical contacts to the SAMs with cone-shaped tips of GaO_x/EGaIn using previously reported methods[42]. All the measurements were performed with the bottom contact connected to the ground and the bias was applied to the EGaIn top electrode from 0 V → +1 V → 0 V → −2 V → 0 V. A Keithley 6430 source meter was used to bias the junction controlled by LabVIEW. The J(V) curves were recorded in steps of 20 mV (Supplementary Section 5). For millisecond and microsecond pulse experiments, a Keysight B1500 Semiconductor Device Analyzer was used to apply the pulse sequences and measure the current output using two RSU heads connected to the B1530A WGFMU (waveform generator fast measurement unit). Voltage pulses of +1 and −2 V were applied for stability measurements with repeated cycling with a pulse duration of 20 µs.

Statistical analysis of J(V) characteristics

All the J(V) data were used to perform the statistical analysis except the unstable and shorted junctions. We defined a junction as unstable when the current value suddenly increased to the compliance limit of our electrometer. The number of consecutive J(V) traces was limited to three traces per junction because of the memory effect on the switching probabilities of the molecules (as explained in the main text). We determined the median averages of the values of $\log_{10}|J|$ along with the median absolute deviations, σ_m, a recommended alternative method as described in Reus et al.[45], because this method does not rely on assumptions as to the distribution of the data. From all $\log_{10}|J|$ values measured at each bias, we calculated the median $\log_{10}|J|$ average, $<\log_{10}|J|>_m$ and σ_m. We created our heatmaps using two-dimensional kernel density estimations with OriginPro 2019b. We used an exact estimation as the density calculation method, a bivariate kernel density estimator as the bandwidth selection method and a grid size of 100. The exact estimation method in OriginPro 2019b calculates the density values based on a bidimensional Gaussian kernel. See the detailed description in Supplementary Section 5.

Synaptic behaviour, Pavlovian learning and logic gates

The measurements of the junctions as an artificial synapse were carried out with samples prepared using the methods described in the SAM formation section above and using a cone-shaped tip of GaO_x/EGaIn as described in Electrodes preparation above. For each junction an initial I(V) measurement was performed, as described in the Junction fabrication and electrical measurements section above to ensure the junction had J(V) characteristics close to the log-median (Supplementary Fig. 15), as given in Supplementary Section 5.2. Following this, sequences of voltage pulses were programmed and applied using a LabView-based software CryoMeas (developed by C. J. B. Ford, University of Cambridge) using a Keithley 6430 source meter that recorded the current simultaneously. A typical pulse sequence used to extract the plasticity depending on the pulse parameters is shown in Fig. 3a, and the custom pulse sequences used for Pavlovian learning are shown and described in Supplementary Section 5.2. Pavlovian learning was demonstrated in a set-up that involved two Keithley 6430 source meters operated simultaneously, as described in the main text (Fig. 4a–e), Extended Data Fig. 7 and Supplementary Section 5.2.2. Pulse parameters used for the logic gates are described in Supplementary Section 5.2.3.

Theoretical modelling of the transport dynamics

We used a theoretical model developed by Migliore and Nitzan[20] to model the junction characteristics and explain our observations. We used the standard single-level quantum model to account for the current through the molecular junction in both the on and off states, which has been shown to effectively describe the conduction through single-molecule junctions, but modified by us to describe the current across large-area molecular junctions[42,46]. The model described above was used to fit the data presented in Fig. 5d–g in the main text. The

detailed description of the mechanistic modelling, Landauer formalism to account for the tunnelling in the on and off states, fitting of the data and related discussion are given in Supplementary Section 6.

Data availability

Data are available in the supplementary materials and on https://dataverse.harvard.edu/privateurl.xhtml?token=efd1a016-cc24-41ab-891b-5217fa6dd56d. Source data are provided with this paper.

Code availability

Codes are available from Harvard Dataverse at https://dataverse.harvard.edu/privateurl.xhtml?token=efd1a016-cc24-41ab-891b-5217fa6dd56d.

References

41. Larsen, C. B. et al. Synthesis and optical properties of unsymmetrically substituted triarylamine hexaazatrinaphthalenes. *Eur. J. Org. Chem.* **2017**, 2432–2440 (2017).
42. Chen, X. et al. Molecular diodes with rectification ratios exceeding 10^5 driven by electrostatic interactions. *Nat. Nanotechnol.* **12**, 797–803 (2017).
43. Yuan, L., Jiang, L., Thompson, D. & Nijhuis, C. A. On the remarkable role of surface topography of the bottom electrodes in blocking leakage currents in molecular diodes. *J. Am. Chem. Soc.* **136**, 6554–6557 (2014).
44. Yuan, L., Breuer, R., Jiang, L., Schmittel, M. & Nijhuis, C. A. A molecular diode with a statistically robust rectification ratio of three orders of magnitude. *Nano Lett.* **15**, 5506–5512 (2015).
45. Reus, W. F. et al. Statistical tools for analyzing measurements of charge transport. *J. Phys. Chem. C* **116**, 6714–6733 (2012).
46. Yuan, L. et al. Transition from direct to inverted charge transport Marcus regions in molecular junctions via molecular orbital gating. *Nat. Nanotechnol.* **13**, 322–329 (2018).

Acknowledgements

Author contributions

C.A.N. conceived and supervised the project. D.T. conducted the atomistic modelling. E.d.B. and C.N. conducted the numerical modelling. Y.W. and A.B. synthesized the compounds, Y.W. and Y.H. performed the CV and ultraviolet–visible measurements. Z.Z. and D.-C.Q. performed the angle-resolved XPS and near-edge X-ray absorption fine structure measurements and analysis. Y.W. and Q.Z. performed the *I–V* electrical measurements. H.P.A.G.A. designed, performed and analysed the synaptic emulation measurements. S.S. and F.A.A. conducted the millisecond-scale pulse experiments. C.H. and B.B. conducted and analysed the sum-generation frequency experiments. A.L. developed the Origin code for electrical data analysis. C.A.N., E.d.B., D.T. and H.P.A.G.A. wrote the manuscript and all the authors commented on it.

Competing interests

The authors declare no competing interests.

Additional information

Extended data is available for this paper at https://doi.org/10.1038/s41563-022-01402-2.

Supplementary information The online version contains supplementary material available at https://doi.org/10.1038/s41563-022-01402-2.

Correspondence and requests for materials should be addressed to Enrique del Barco, Damien Thompson or Christian A. Nijhuis.

Peer review information *Nature Materials* thanks Ferdinand Grozema, Tae-Woo Lee and the other, anonymous, reviewer(s) for their contribution to the peer review of this work.

Reprints and permissions information is available at www.nature.com/reprints.
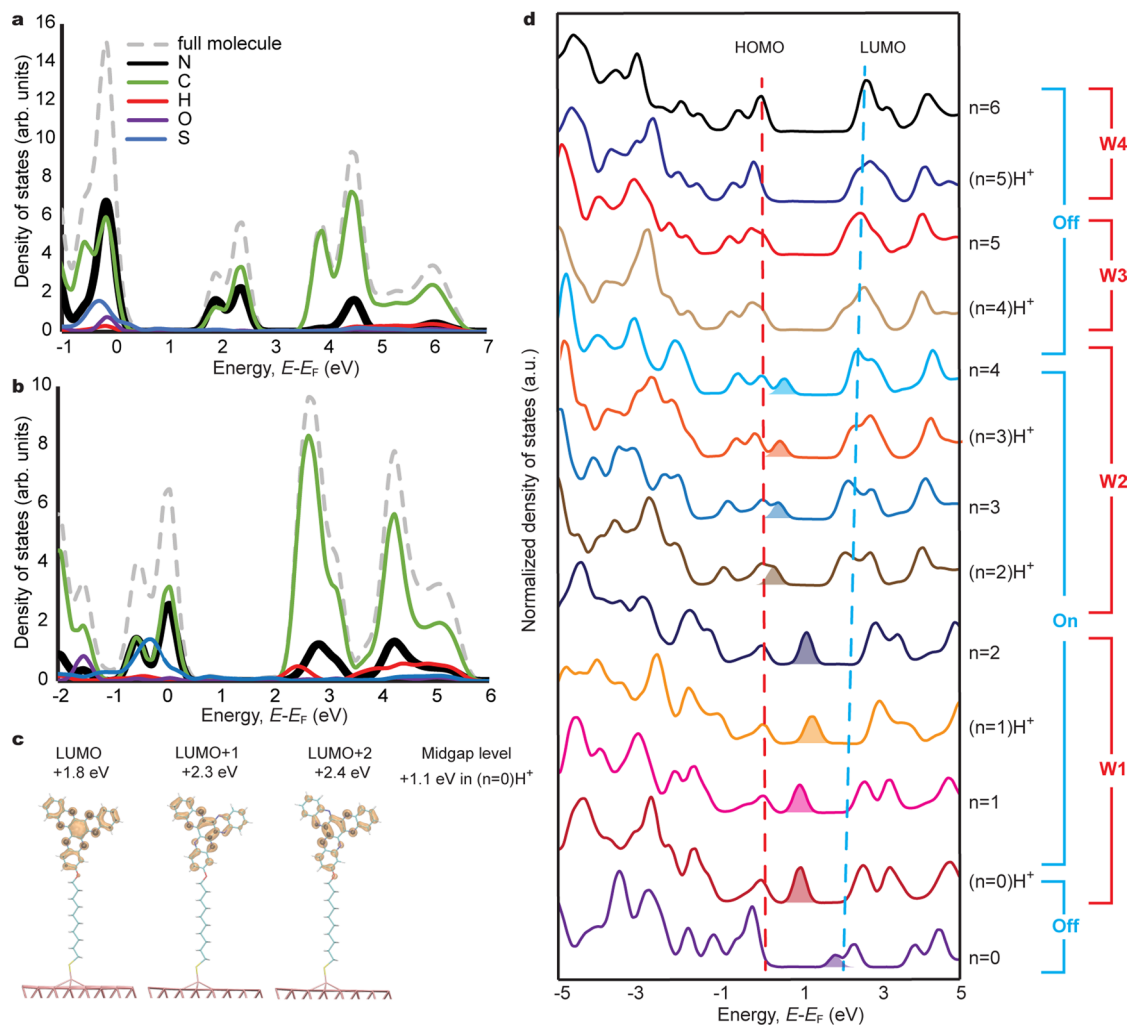
Extended Data Fig. 1 | The periodic DFT calculations. a, The calculated PDOS of Au-bound S-C_{10}-HATNA with the nitrogen sites plotted as a thick black line. The full molecule is shown as a dashed grey line and contributions from carbon, hydrogen, oxygen, and sulphur sites are plotted as green, red, purple, and blue lines, respectively. **b**, The calculated PDOS of post-PCET Au-S-C_{10}-(H_6-HATNA).

(**c**) Computed surfaces of the empty electron-acceptor LUMO → LUMO + 2 levels in Au-S-C_{10}-HATNA together with the mid-gap state created at +1.1 eV in the first protonation step generating Au-S-C_{10}-H^+-HATNA. **d**, The calculated PDOS on the molecule of HATNA SAMs on Au(111) for all oxidation and protonated states.
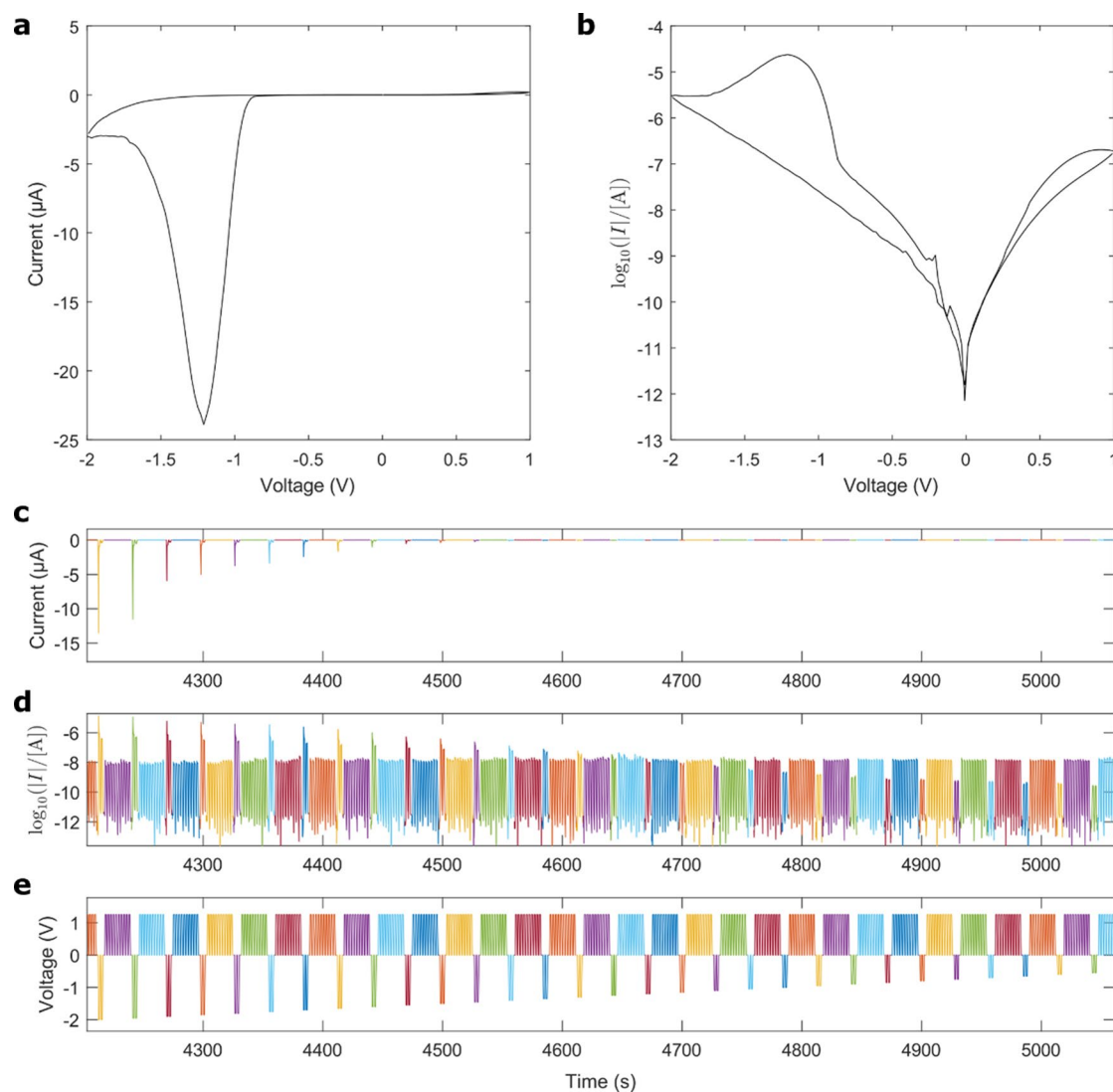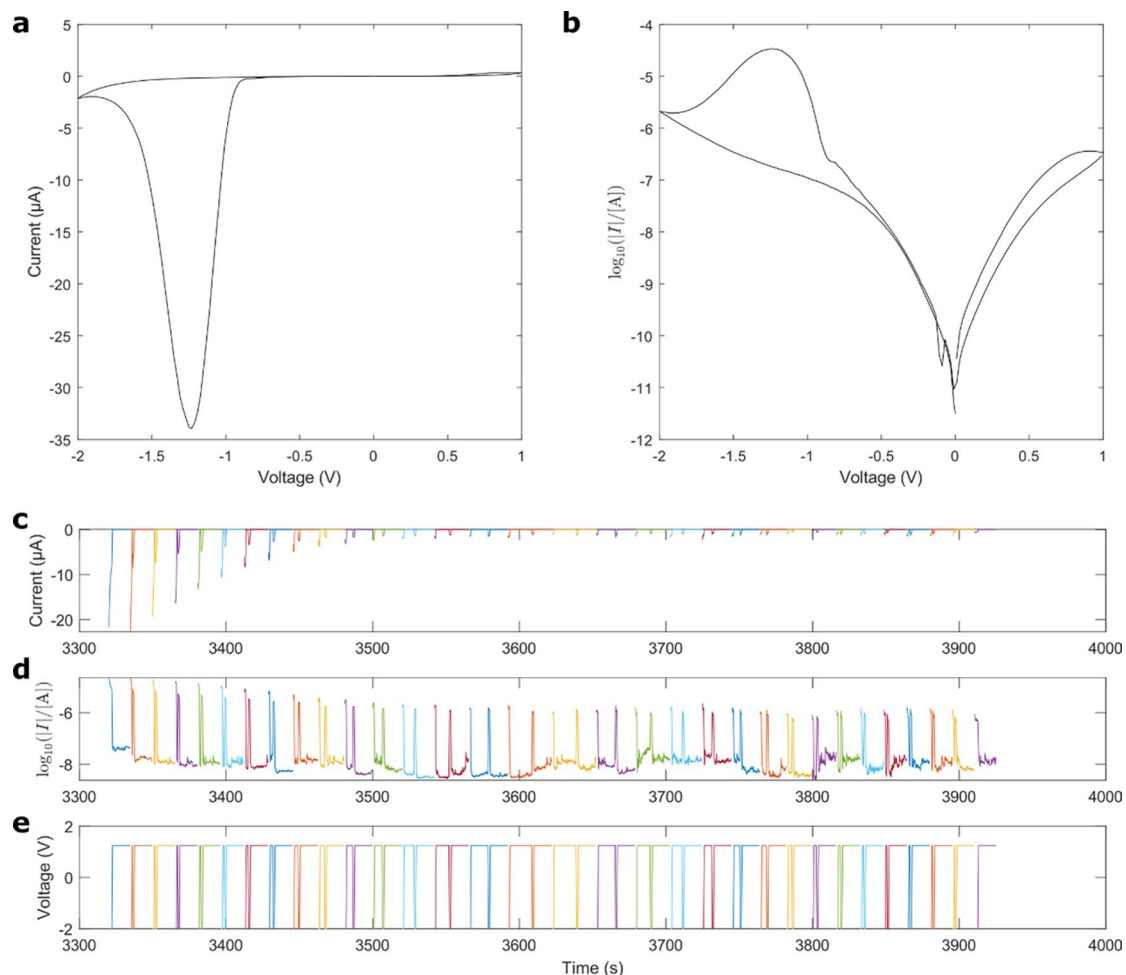
Extended Data Fig. 2 | Measurement of potentiation as a function of negative pulse amplitude as shown in Fig. 5b. a-b, $I(V)$ profile of the junction used in the measurement in linear (**a**) and logarithmic scale (**b**). **c-e,** pulse sequence used in the measurement with current (**c**), logarithm of current (**d**) and voltage (**e**) as a function of time, with colour used to help distinguish sections of the sequence. A first negative voltage pulse of amplitude V_p (with $t_p = 1$ s) was applied, a delay at 0 V was set for $t_d = 1$ s, and then a second negative voltage pulse of magnitude V_p was applied, followed by a series of positive voltage pulses of amplitude $V_r = 1.25$ V to reset the junction. This sequence was repeated each time varying the amplitude of the negative voltage pulses V_p from 0.5 V to 2 V and back. After half a sequence to train the junction, the current amplitude of the second negative pulse was compared to that of the first negative pulse (using the first data point of each pulse) to determine the potentiation as a function of V_p. Time $t = 0$ corresponds to the time the measurement was started, immediately after junction formation.
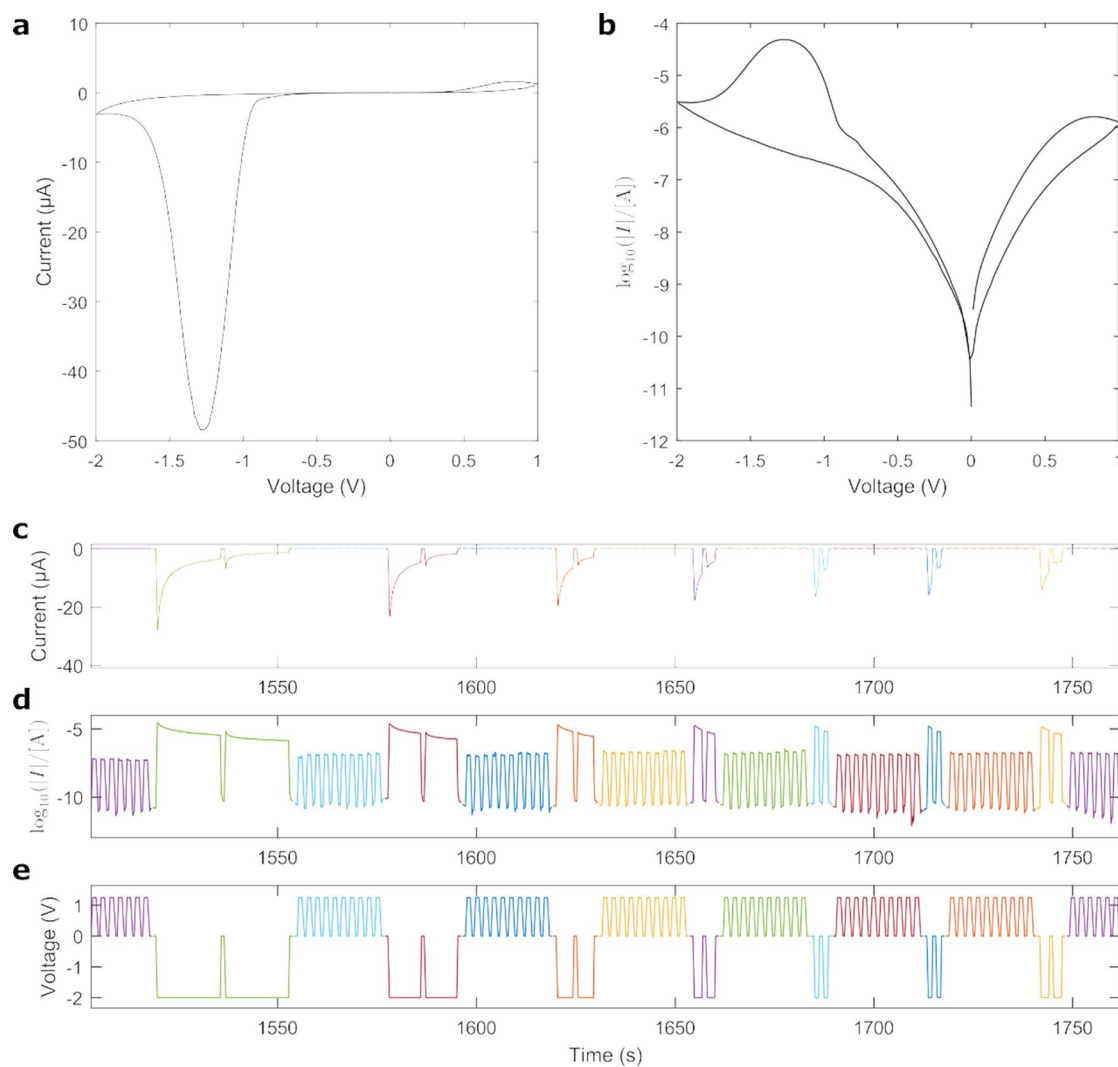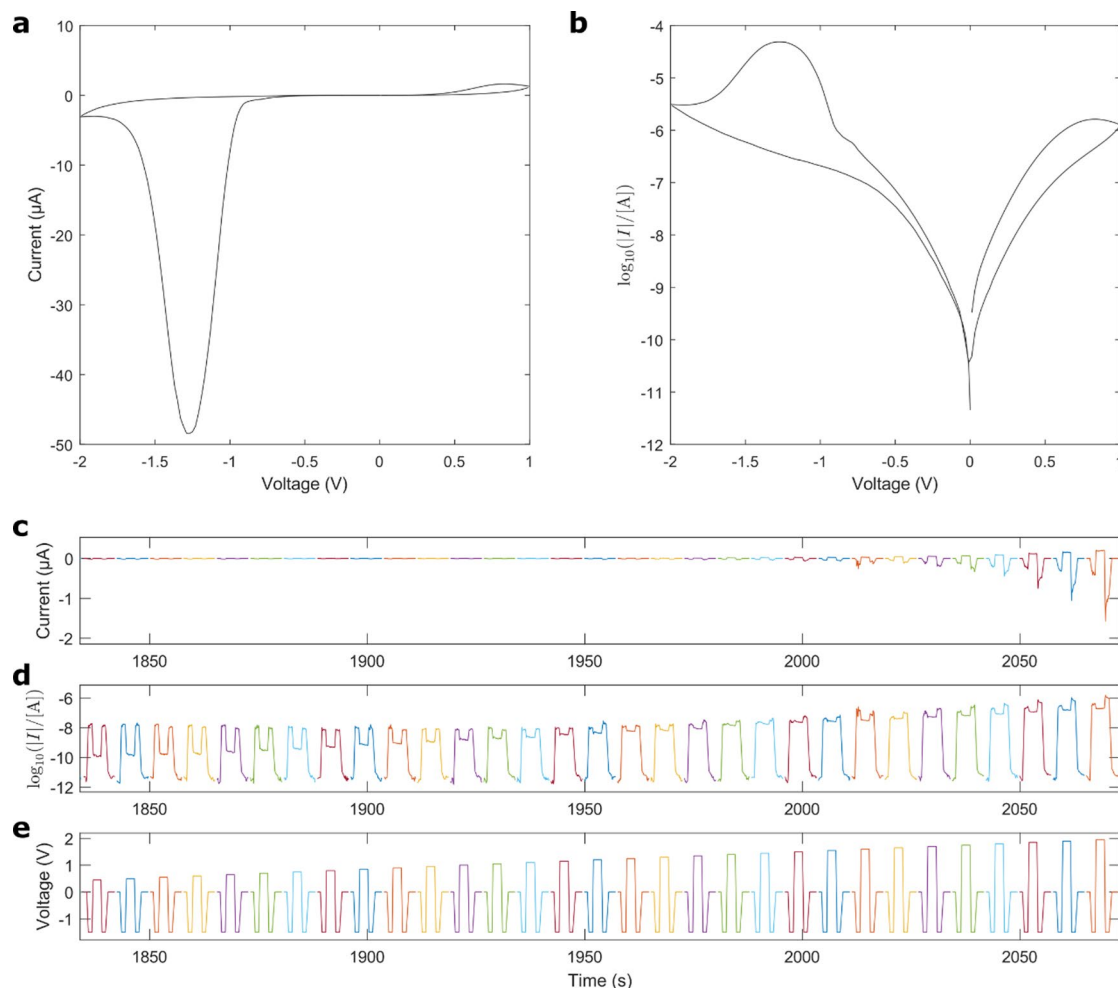
Extended Data Fig. 3 | Measurement of potentiation as a function of negative pulse duration as shown in Fig. 5c. **a-b**, $I(V)$ profile of the junction used in the measurement in linear (**a**) and logarithmic scale (**b**). **c-e**, pulse sequence used in the measurement with current (**c**), logarithm of current (**d**) and voltage (**e**) as a function of time, with colour used to help distinguish sections of the sequence. A first negative voltage pulse of amplitude $V_p = -2V$ and duration t_p was applied, a delay at 0 V was set for $t_d = 1$ s, a second negative voltage pulse of magnitude V_p was applied, followed by a series of positive voltage pulses of amplitude $V_r = 1.25$ V to reset the junction. This sequence was repeated each time varying V_p the amplitude of the negative voltage pulses from 0.5 V to 2 V and back, and after half a sequence to train the junction, the current amplitude of the second negative pulse was compared to that of the first negative pulse to determine the potentiation as a function of V_p. Time $t = 0$ corresponds to the time the measurement was started, immediately after junction formation.

Extended Data Fig. 4 | Measurement of potentiation as a function of inter-pulse delay t_d as shown in Fig. 5d. a-b, $I(V)$ profile of the junction used in the measurement in linear (**a**) and logarithmic scale (**b**). **c-e,** pulse sequence used in the measurement with current (**c**), logarithm of current (**d**) and voltage (**e**) as a function of time, with colour used to help distinguish sections of the sequence. A first negative pulse was applied, followed by a delay of duration t_d at 1.25 V, then a second pulse, and finally a positive pulse is applied to reset the junction. Each pulse pair was used to extract two data points: one with $t_d > 0$ and one with $t_d < 0$, whereby a positive (negative) value of t_d signifies that the reference pulse occurs before (after) the measured pulse. The relative potentiation was measured as the ratio of the difference between the current of the measured pulse and the current of the reference pulse (here using the values of current in the middle of the pulses) to the current of the reference pulse. Time $t = 0$ corresponds to the time the measurement was started, immediately after junction formation.

Extended Data Fig. 5 | Measurement of potentiation as a function of positive pulse duration as shown in Fig. 5e. a-b, $I(V)$ profile of the junction used in the measurement in linear (**a**) and logarithmic scale (**b**). **c-e**, pulse sequence used in the measurement with current (**c**), logarithm of current (**d**) and voltage (**e**) as a function of time, where colour is used to help distinguish sections of the sequence. A negative reference voltage pulse (V_p = -1.5 V, t_p = 1 s) was applied, a positive voltage pulse of varying amplitude (duration t_d = 2 s) was applied, and a second negative voltage pulse (V_p = -1.5 V, t_p = 1 s) was applied. This sequence was repeated each time varying V_r the amplitude of the positive voltage pulse from 0.5 V to 2 V and back, and after one training sequence (~500 s), the current amplitude of the second negative pulse was compared to that of the reference negative pulse to determine the potentiation as a function of V_r. Time t = 0 corresponds to the time the measurement was started, immediately after junction formation.
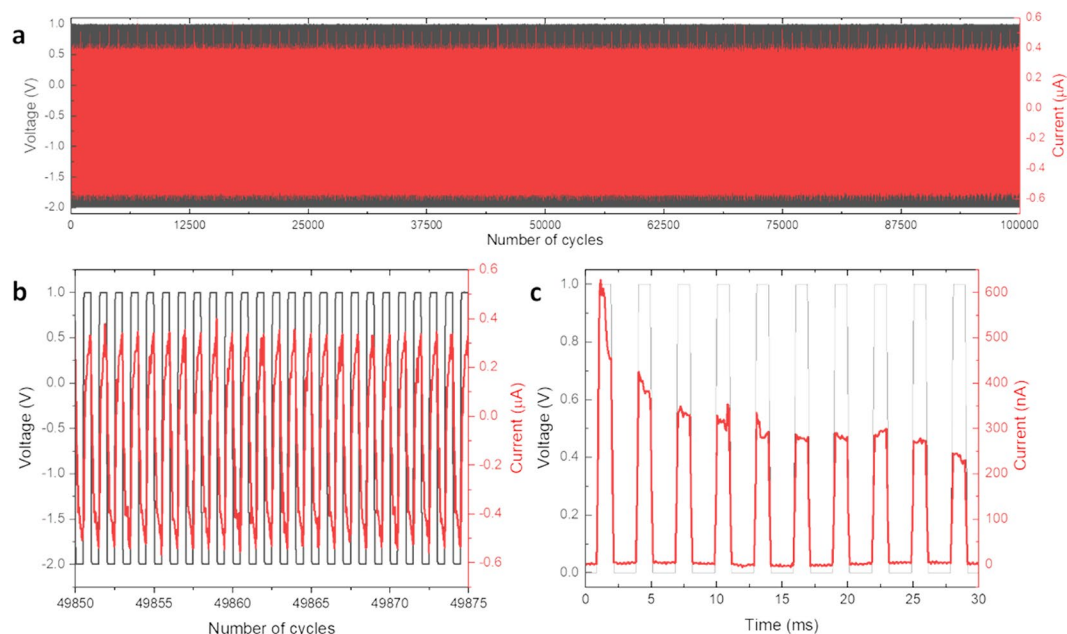
Extended Data Fig. 6 | Voltage cycling measurements for the junctions. Voltage cycling showing 100 000 voltage pulses with amplitudes of -2 V and +1 V and pulse time of 20 µs (black) and current response (red); **b**, zoomed-in version of the voltage cycling data in **a** to show the pulse parameters and current response more clearly; **c**, Measurement of potentiation as a function of short positive voltage pulses of +1 V amplitude and 2 ms pulse time period (black), and corresponding current response of the junction (red) showing PPD. Due to the basic nature of HATNA, HATNA can be protonated representing the on-state (that is, the $(HATNA)H^+$ state as explained in the main text and shown in Fig. 2f-g (and experimentally proven with vibrational sum-frequency generation spectroscopy of HATNA monolayers described in Supplementary Section S3.3). A series of short positive voltages deprotonates HATNA turning it off which is observed as reduction in the current response, as seen here. More experimental details on the pulse parameters are given in Supplementary Information Section S5.3.
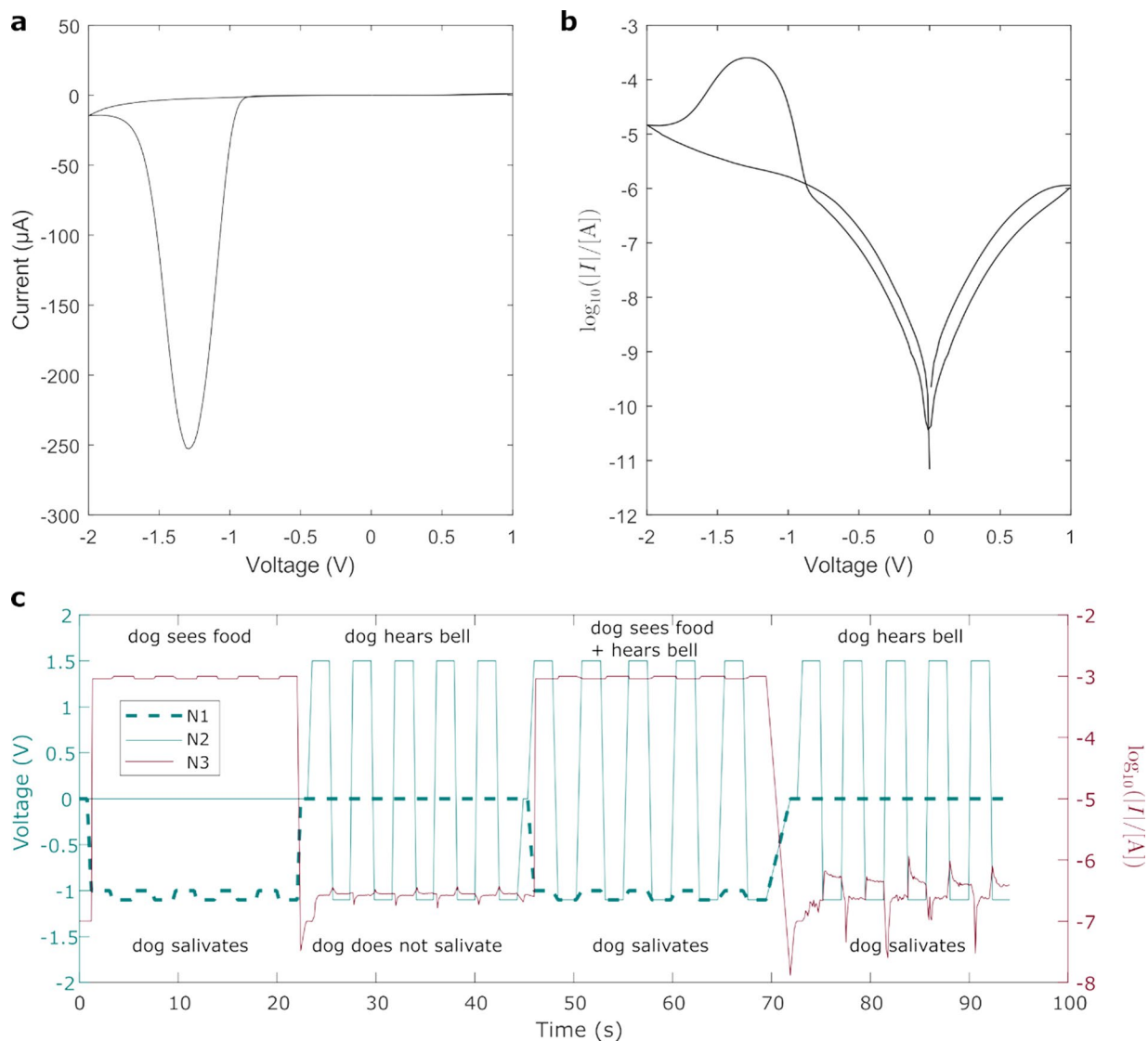
Extended Data Fig. 7 | Measurement demonstrating the Pavlov experiment (Hebbian learning). a-b, $I(V)$ profile of the junction used in the measurement in linear (**a**) and logarithmic scale (**b**). **c**, pulse sequence showing Hebbian learning (from Fig. 6b-e). The e-ANN works as follows: two source-measure units represent two artificial neurons N1 and N2 delivering voltage inputs in separate channels feeding into a third channel (see Fig. 6a) N3 where the current received is the output. N1 is connected via a fixed resistor (1kΩ) to N3 and gives the output unconditionally. N2 includes the junction in the off state such that pulses from N2 do not initially result in a substantial signal in N3. It corresponds to 'dog hears bell'. However, firing pulses in N1 and N2 results in a PPF process in N2, 'training' it to deliver an output in N3 when pulses are fired from N2 thereafter. The sequences of voltage pulses are as follows. N1 alternates between pulses at -1 V and -1.1 V, each lasting 2 s, repeated 5 times. N2 alternates between pulses at +1.5 V and -1.1 V, each lasting 2 s, repeated 5 times. When pulses are applied from N1 and N2 simultaneously, the voltage across the dynamic switch can be estimated to be alternating between +2.4 V and -0.1 V approximately, according to Kirchhoff's circuit laws, which excites the junction (enhances its conductance) and thus the coupling to N3.
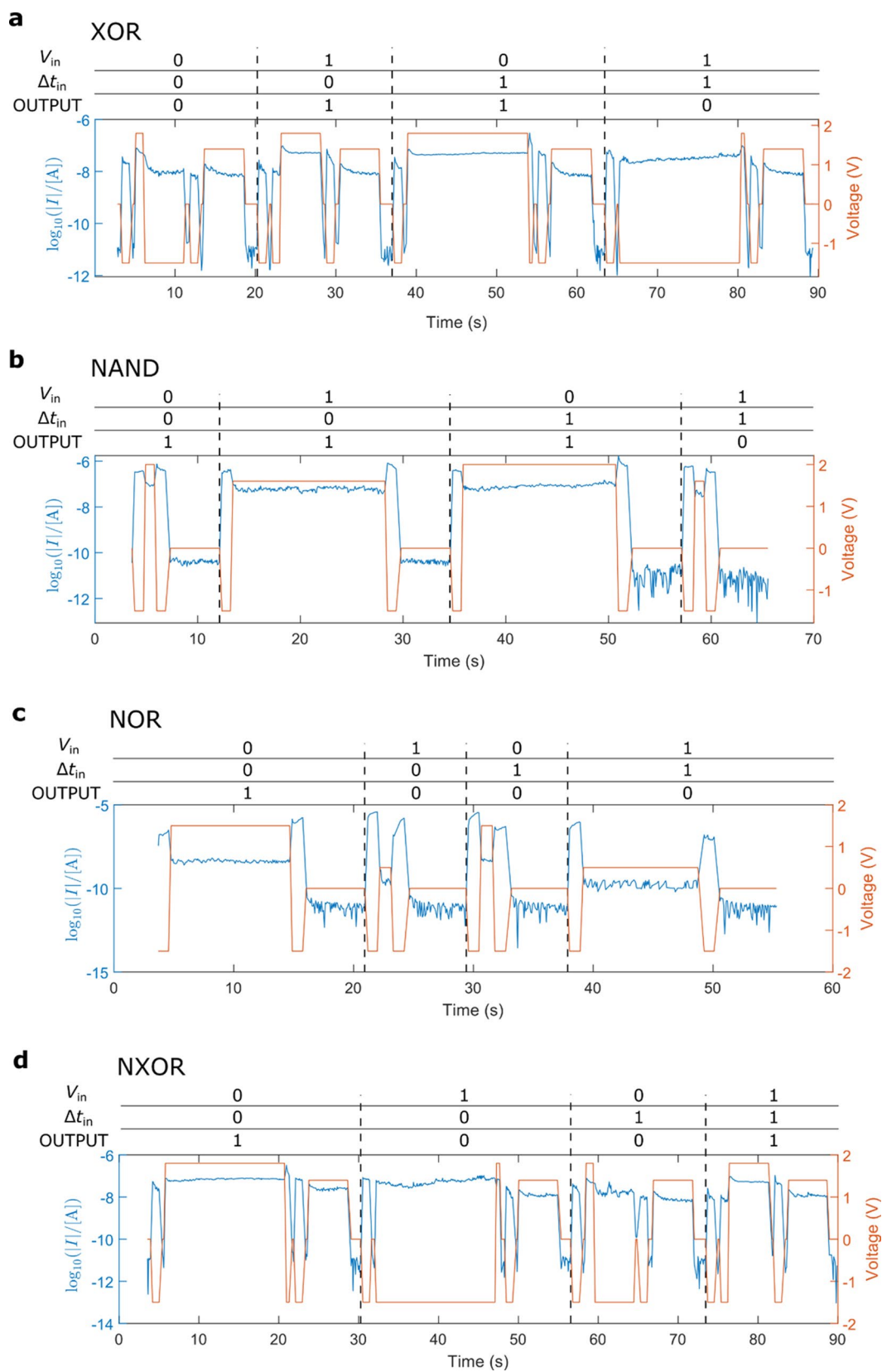
Extended Data Fig. 8 | Demonstration of remaining logic gates. a, XOR; **b**, NAND; **c**, NOR; **d**, NXOR, as per the operation system described in the main text and Fig. 6, with current and voltage traces and truth tables. More details on the pulse parameters are given in Supplementary Information Section S5.2.3.